A study of the inspiral-merger-ringdown consistency test with gravitational-wave signals from compact binaries in eccentric orbits

Md Arif Shaikh,[1,2,3,*,†] Sajad A. Bhat,[4,5,*,‡] and Shasvath J. Kapadia[4,§]

[1]Department of Physics, Vivekananda Satavarshiki Mahavidyalaya (affiliated to Vidyasagar University),
Manikpara 721513, West Bengal, India
[2]Department of Physics and Astronomy, Seoul National University, Seoul 08826, Korea
[3]International Centre for Theoretical Sciences,
Tata Institute of Fundamental Research, Bangalore 560089, India
[4]The Inter-University Centre for Astronomy and Astrophysics,
Post Bag 4, Ganeshkhind, Pune 411007, India
[5]Chennai Mathematical Institute, Plot H1 SIPCOT IT Park, Siruseri 603103, India

(Received 27 February 2024; accepted 4 June 2024; published 12 July 2024)

The inspiral-merger-ringdown consistency test (IMRCT) is one among a battery of tests of general relativity (GR) employed by the LIGO-Virgo-KAGRA (LVK) Collaboration. It is used to search for deviations from GR in detected gravitational waves (GWs) from compact binary coalescences (CBCs) in a model-agnostic way. The test compares source parameter estimates extracted independently from the inspiral and postinspiral portions of the CBC signals and, therefore, crucially relies on the accurate modeling of the waveform. Current implementations of the IMRCT routinely use quasicircular waveforms, under the assumption that the residual eccentricity of the binary when the emitted GWs enter the frequency band of the LVK detector network will be negligible. In this work, we perform a detailed study to investigate the typical magnitudes of this residual eccentricity that could potentially lead to spurious violations of the IMRCT. To that end, we conduct injection campaigns for a range of eccentricities and recover with both quasicircular and eccentric waveforms. We find that an eccentric GW signal from a GW150914-like system with eccentricity $e_{\mathrm{gw}} \gtrsim 0.04$ at an orbit averaged frequency $\langle f_{\mathrm{ref}} \rangle = 25$ Hz breaks the IMRCT if recovered with quasicircular waveforms at $\gtrsim 68\%$ CL. The violation becomes more severe ($\gtrsim 90\%$ confidence) for $e_{\mathrm{gw}} = 0.055$ at $\langle f_{\mathrm{ref}} \rangle = 25$ Hz. On the other hand, when eccentric waveforms are used, the IMRCT remains intact for all eccentricities considered. We also briefly investigate the effect of the magnitude and orientation (aligned/antialigned) of the component spins of the binary on the extent of the spurious violations of the IMRCT. Our work, therefore, demonstrates the need for accurate eccentric waveform models in the context of tests of GR.

DOI: 10.1103/PhysRevD.110.024030

I. INTRODUCTION

The LIGO-Virgo [1,2] network of ground-based interferometric gravitational-wave (GW) detectors has detected ~90 compact binary coalescence (CBC) events in its first three observing runs (O1, O2, O3) [3]. The majority of these are binary black hole (BBH) mergers, although binary neutron star [4,5] and neutron star-black hole coalescences [6] have also been observed.

The detected GW signals, especially those pertaining to BBH mergers, come from the last few orbits of the inspiral, as well as the merger and ringdown phases (see, e.g., [7]). These GWs are well suited to probe general relativity (GR) in the strong-field regime, unlike most tests of GR that use electromagnetic waves, which typically probe the weak field regime.[1]

The LIGO-Virgo-KAGRA (LVK) Collaboration [1,2,10] has conducted a suite of tests of GR across O1, O2, and O3 [11]. This includes[2]

(1) A model-agnostic residuals test, which subtracts out the best-matched GR-modeled CBC waveform from the data containing the GW signal, and checks if the

---

[*] These authors contributed equally to this work.
[†] arifshaikh.astro@gmail.com
[‡] sajad.bhat@iucaa.in
[§] shasvath.kapadia@iucaa.in

[1] A notable exception to this is the results of the Event Horizon Telescope [8], which imaged the shadow of the supermassive black hole at the center of the M31 galaxy and enabled electromagnetic-based strong-field tests of GR [9].

[2] But is not limited to.

statistical properties of the residual are consistent with noise [12–14].

(2) A test that probes the inspiral evolution of the CBC by searching for deviations in Post-Newtonian (PN) parameters of the GW signal [15–22].

(3) An inspiral-merger-ringdown consistency test (IMRCT) that compares and assesses the consistency between the low- and high-frequency portions of the CBC signals [23,24].

(4) Propagation tests of GWs that compare their speed with respect to the speed of light [25] as well as any modulations in the waveform due to finite-graviton-mass-driven velocity dispersion [26].

In this work, we restrict our attention to the IMRCT. The IMRCT compares the two-dimensional joint posterior on the final mass and spin of the merged binary estimated independently from the inspiral (low-frequency) and post-inspiral (high-frequency) portions of the waveform [23,24]. A sufficiently large deviation from GR should result in the difference distribution between final mass and final spin evaluated from these 2D posteriors to deviate from the origin (zero). However, it is conceivable that waveforms that do not accurately capture the physics of the CBC could lead to biased posteriors. We propose to study the resulting systematics in the IMRCT. In particular, we investigate how the neglect of eccentricity in the waveform models could cause spurious violations of this test.

It is well known that, as GWs carry away energy and angular momentum of a CBC, it reduces the binary orbit's eccentricity [27,28]. The prevalent expectation is that by the time GWs from the CBC enter the frequency band of the LVK network, any initial eccentricity that the binary may have had at the time of formation would have been reduced to a negligibly small value. Indeed, current constraints on the rate of eccentric mergers, from searches for such signals, suggest that observations of these in O4 are likely to be relatively rare [29–31]. Thus, tests of GR conducted so far by the LVK routinely use quasicircular waveforms, including the IMRCT.

On the other hand, certain formation channels, such as those pertaining to dense stellar environments, could produce binaries whose eccentricities are non-negligible when they enter the LVK frequency band [32]. Dynamical encounters in such environments could harden the binary so that GW emission cannot completely carry away the eccentricity by the time the GWs enter the LVK's frequency band [33–35]. Moreover, in active galactic nuclei disks, eccentricity can be amplified by binary-single encounters [36,37], while the presence of a third object in the vicinity of the binary could similarly boost the eccentricity via the Kozai-Lidov mechanism [38–44]. Such eccentricity-enhancing processes could also leave a residual in-band eccentricity detectable by the LVK network. Neglecting eccentricity of such signals in (PN) parametrized tests has already been shown to lead to spurious violations of GR both at the individual event level [45] and population level inference [46]. We here focus only on the effect of neglect of eccentricity on the IMRCT.

Performing the IMRCT using quasicircular waveform models, could potentially cause systematics in the IMRCT. Intuitively, the eccentricity at the time of band entry of the GW signal will be larger than the eccentricity in the postinspiral phase, where it is usually vanishingly small. Thus, one would expect source parameters recovered with quasicircular waveform models to be biased when using the inspiral portion of the waveform [47–49], while those recovered using the postinspiral phase to be relatively less biased, if at all. The resulting 2D difference distribution constructed from the (inspiral/postinspiral) final mass and spin posteriors should be deviated from zero.

To assess the impact of neglecting eccentricity in waveform models on the IMRCT, we consider a set of synthetic eccentric GW signals. We inject these in the most probable realization of (zero-mean) Gaussian noise, the so-called "zero-noise" realization,[3] assuming an O4-like noise power-spectral density (PSD) [50]. We then perform the IMRCT on each of these signals, using quasicircular templates. We find that the IMRCT is indeed violated with quasicircular templates, as we increase the injected eccentricity, for a set of masses and spins where the IMRCT is known not to suffer from other systematics. This violation progressively increases, from moderate to severe, with increasing eccentricity. To ascertain that no intrinsic waveform systematics are contributing to this bias, we repeat the IMRCT using eccentric waveform model for recovery. We indeed find that the IMRCT is no longer violated.

Past work, using an approximate Fisher matrix analysis [51] and the Cutler-Vallisneri framework [52], pointed out that the IMRCT could be violated due to neglect of eccentricity [53]. Another work also found spurious violations of the IMRCT using available numerical-relativity waveforms as injections, while performing the IMRCT with quasicircular phenomenological waveform models [54]. Our work complements and expands on both of these studies in the following way. We perform Bayesian parameter inference runs using a large-scale nested sampler and, therefore, have a more realistic estimate of the bias compared to those in provided in [53]. Moreover, unlike in [53], we do not neglect the eccentricity in the postinspiral part of the signal which may lead to overestimation or underestimation of the bias. Also, because we employ an eccentric waveform model `TEOBResumS-Dalí` [55,56], we have two advantages over the results in [54]. We use the same waveform model to create the injection and then to recover it. Therefore, we rule out any bias originating due to the waveform

---

[3] Here zero-noise realization refers to the most-probable realization of Gaussian noise with zero mean, and the parameter uncertainties obtained using this noise-realization provide lower bound to the estimates obtained using the nonzero real noise realization.

systematics which may be present if the recovery template is not as accurate as the injected numerical relativity (NR) waveforms. Also, we have the freedom to create injections at arbitrary values of eccentricities allowing us to do an injection study on a finer grid of eccentricity values. This, in turn, allows us to identify more accurately at what eccentricity the IMRCT bias becomes severe. Similarly, we examine the sensitivity of the bias for a given eccentricity on other parameters like the magnitude of the component spins and their orientation (aligned/antialigned) with respect to the orbital angular momentum of the binary. Moreover, we ascertain that the IMRCT is indeed recovered as expected, when eccentricity is included, for all eccentricities considered. We make contact with both these works to compare the eccentricity at which the IMRCT is violated, using a generalized definition of eccentricity that is independent of waveform models [57].

The rest of this paper is organized as follows. Section II briefly describes the IMRCT, and argues why one should expect spurious violations due to neglect of eccentricity. Section III shares the results of the injection campaign described above. Section IV summarizes the work and discusses other potential sources of spurious IMRCT violations.

II. METHODS

A. Gravitational-wave parameter estimation

In GR, GWs have two polarizations, h_+ and $h_\times$. The phase evolution of these polarizations depends on the intrinsic parameters of the binary, viz. the masses m_1, m_2 of the individual components[4] and the spin vectors of these components $\mathbf{S}_1$, $\mathbf{S}_2$. The amplitude of the polarizations depends on the inclination of the binary with respect to the line of sight, ι; luminosity distance d_L; the phase ϕ_c; and time t_c at coalescence. In addition to the above mentioned intrinsic parameters, we need two more parameters—eccentricity e and mean anomaly l[5]—at a given reference frequency to accurately describe GWs from a binary in eccentric orbit. Also, the GW waveform shape is more sensitive to the "chirpmass" $\mathcal{M}_c = m_1^{3/5} m_2^{3/5}/(m_1 + m_2)^{1/5}$ compared to individual masses, and often it is more practical to use $\mathcal{M}_c$ and the mass ratio $q = m_1/m_2$ instead of m_1 and m_2 for parameter estimation (PE) [51].

The response of the GW detector to each of the GW polarizations is given by the antenna pattern functions, $F_+, F_\times$. These depend on the location of the source in the sky, viz. the right ascension α and declination δ, as well as the polarization angle ψ. The GW strain measured by the detector is a linear combination of the two polarizations, weighted by the antenna pattern functions

$$h(t;\vec{\theta},\vec{\lambda}) = F_+(\vec{\lambda}_F) h_+(t;\vec{\theta},\vec{\lambda}_h) + F_\times(\vec{\lambda}_F) h_\times(t;\vec{\theta},\vec{\lambda}_h), \quad (1)$$

with t as the detector-frame time, $\vec{\theta} = \{\mathcal{M}_c, q, \mathbf{S}_1, \mathbf{S}_2, e, l\}$, $\vec{\lambda}_F = \{\alpha, \delta, \psi\}$, $\vec{\lambda}_h = \{d_L, \iota, t_c, \phi_c\}$, and $\vec{\lambda} = \vec{\lambda}_F \cup \vec{\lambda}_h$.

Given two waveforms $h_{1,2}(t;\vec{\theta},\vec{\lambda})$, their noise-weighted inner product is defined as

$$\langle h_1, h_2 \rangle = 4\Re \int_{f_{\min}}^{f_{\max}} \frac{\tilde{h}_1^\star(f;\vec{\theta},\vec{\lambda}) \tilde{h}_2(f;\vec{\theta},\vec{\lambda})}{S_n(f)} df, \quad (2)$$

where f is the frequency, and $\tilde{h}_{1,2}$ are Fourier transforms of the corresponding time domain waveforms, $\star$ represents complex conjugation, and $\Re$ denotes the real part. $S_n(f)$ is the noise PSD of the detector. The lower and the upper cutoff frequencies, $f_{\min}$ and $f_{\max}$ are determined by the source properties and the sensitivity of the detector.

Let us now consider a time-domain stretch of detector strain data,

$$s(t) = n(t) + h(t;\vec{\theta},\vec{\lambda}), \quad (3)$$

known to consist of noise $n(t)$ and GW signal $h(t;\vec{\theta},\vec{\lambda})$ whose parameters $\vec{\theta},\vec{\lambda}$ are to be estimated. This can be achieved by sampling the seventeen-dimensional GW posterior $p(\vec{\theta},\vec{\lambda}|s) \propto p(\vec{\theta},\vec{\lambda}) p(s|\vec{\theta},\vec{\lambda})$, where $p(\vec{\theta},\vec{\lambda})$ is the prior distribution on the parameters, and the GW likelihood is given by [51]

$$p(s|\vec{\theta},\vec{\lambda}) \propto \exp\left[-\frac{\langle s - h(\vec{\theta},\vec{\lambda}), s - h(\vec{\theta},\vec{\lambda})\rangle}{2}\right]. \quad (4)$$

The sampling of this high-dimensional posterior is typically achieved using large-scale Markov-chain Monte Carlo methods, or nested-sampling methods.

B. The inspiral-merger-ringdown consistency test

The IMRCT can be thought of as a coarse-grained test of the frequency evolution of a BBH waveform. It compares the low-frequency and high-frequency portions of the waveform by comparing the final mass and spin of the merged binary estimated from the inspiral and merger-ringdown regimes. Let M_f^{I} and $\chi_f^{\mathrm{I}} \equiv |S_f^{\mathrm{I}}|/(M_f^{\mathrm{I}})^2$ be the estimates of the detector-frame final mass and dimensionless spin of the merged binary, respectively, from the inspiral and M_f^{MR}, χ_f^{MR} be the same from the postinspiral part. The IMRCT constructs a joint distribution on the following difference parameters [23,24]:

$$\frac{\Delta M_f}{\bar{M}_f} \equiv 2\frac{M_f^{\mathrm{I}} - M_f^{\mathrm{MR}}}{M_f^{\mathrm{I}} + M_f^{\mathrm{MR}}}, \qquad \frac{\Delta \chi_f}{\bar{\chi}_f} \equiv 2\frac{\chi_f^{\mathrm{I}} - \chi_f^{\mathrm{MR}}}{\chi_f^{\mathrm{I}} + \chi_f^{\mathrm{MR}}}. \quad (5)$$

---

[4] Strictly, the masses that determine the shape of the GW signal measured at the detector are the so-called "detector-frame" masses, which are simply the masses multiplied by $(1+z)$, where z is the cosmological redshift.

[5] The angle variable that describes the position of the compact objects on the orbit can be also described by other equivalent variables like eccentric anomaly or true anomaly [58].

The joint distribution on these parameters should be consistent with zero if the waveform model used to extract the signal in the data captures all the physics associated with the production of the signal. On the other hand, a sufficiently large deviation from GR is expected to shift this distribution to an extent that it does not contain zero with high confidence ($\gtrsim 68\%$ or $\gtrsim 90\%$). In this work, we demonstrate that even if both the waveform model and the signal in the data are consistent with GR, an eccentric signal recovered with a quasicircular model will also lead to a (spurious) violation of the IMRCT.

The estimate of the final mass and final spin of the merged binary determined with the intrinsic parameters $\vec{\theta}$ extracted from the inspiral portion of the waveform is achieved via numerical-relativity-based fits [59–61], as done in [23,24]. On the other hand, the shape of the ringdown contained in the postinspiral portion of the waveform depends on the final mass and spin, which can therefore be extracted directly.

In this work, we restrict ourselves to nonprecessing waveforms, i.e., waveforms produced by binaries whose spin vectors are aligned or antialigned with the orbital angular momentum vector $\mathbf{L}$ (z axis). Moreover, we only consider binaries with mass ratios q that are close to 1 ($q = m_1/m_2 \sim 1$). We therefore only need to use the leading order $(2, \pm 2)$ multipole, since higher multipoles for the types of systems we consider will be suppressed.

The choice of the transition frequency that separates the inspiral and postinspiral portions of the waveform is not unique. However, all implementations of the IMRCT use some approximation of the frequency corresponding to the innermost stable circular orbit (ISCO) of the binary. The LVK estimates the ISCO using the medians of intrinsic parameters θ extracted from the full inspiral-merger-ringdown waveform. Narayan *et al.* [54] use the medians of the final mass and spin of the merged binary estimated from the full inspiral-merger-ringdown waveform, similar to what was originally done in [23,24]. However, as pointed out in [23,24,54], the IMRCT is largely insensitive to moderate variations in the choice of the transition frequency. In this work, we use the exact values of $\vec{\theta}$ (i.e., the injected values), as well as the numerical relativity fits [59–61], to determine a point estimate of the final mass and spin, from which the ISCO frequency is evaluated.

C. A standardized definition of eccentricity

In GR, there is no universally agreed upon definition of eccentricity. Consequently, different waveform models adopt custom internal definitions of eccentricity, leading to model-dependent inferences about eccentricity. To mitigate ambiguity in the inferred value of eccentricity from gravitational wave data analysis, there is a growing effort to standardize the definition of eccentricity. This standardization involves measuring eccentricity from a gauge-independent quantity, such as the gravitational waveform modes [56,57,62–67].

The waveform modes are obtained from the polarizations by decomposing the complex combination $h_+ - ih_\times$ on a sphere into a sum of spin-weighted spherical harmonic modes $\mathfrak{h}_{\ell m}$, so that the waveform along any direction (ι, φ_0) in the binary's source frame is given by

$$\mathfrak{h}(t, \iota, \varphi_0) = \sum_{\ell=2}^{\ell=\infty} \sum_{m=-\ell}^{m=\ell} \mathfrak{h}_{\ell m}(t)\, {}_{-2}Y_{\ell m}(\iota, \varphi_0), \tag{6}$$

where ι and φ_0 are the polar and azimuthal angles on the sky in the source frame, and ${}_{-2}Y_{\ell m}$ are the spin $= -2$ weighted spherical harmonics.

In this work, we employ the `Python` implementation `gw_eccentricity` of the standardized definition of eccentricity from [57], which defines the eccentricity $e_{\rm gw}$ using the frequency of the (2, 2) mode $\mathfrak{h}_{22}$. Initially, it computes $e_{\omega_{22}}$ as described in [57,63,64,66]:

$$e_{\omega_{22}}(t) = \frac{\sqrt{\omega_{22}^{\rm p}(t)} - \sqrt{\omega_{22}^{\rm a}(t)}}{\sqrt{\omega_{22}^{\rm p}(t)} + \sqrt{\omega_{22}^{\rm a}(t)}}. \tag{7}$$

Here, $\omega_{22}^{\rm p}(t)$ and $\omega_{22}^{\rm a}(t)$ denote the interpolants through the frequency of the (2, 2) mode at the pericenter (point of closest approach) and the apocenter (point of farthest approach), respectively. The frequency ω_{22} of the (2, 2) mode is derived from $\mathfrak{h}_{22}$ as

$$\mathfrak{h}_{22}(t) = A_{22}(t) e^{-i\phi_{22}(t)}, \tag{8}$$

$$\omega_{22}(t) = \frac{\mathrm{d}\phi_{22}(t)}{\mathrm{d}t}. \tag{9}$$

After computing $e_{\omega_{22}}$ from $\mathfrak{h}_{22}$, $e_{\rm gw}$ is determined through the following transformation to ensure that $e_{\rm gw}$ correctly exhibits the Newtonian limit [67],

$$e_{\rm gw} = \cos(\Psi/3) - \sqrt{3}\sin(\Psi/3), \tag{10}$$

where

$$\Psi = \arctan\left(\frac{1 - e_{\omega_{22}}^2}{2 e_{\omega_{22}}}\right). \tag{11}$$

Since eccentricity decays via gravitational wave radiation, we must specify a reference frequency where the value of $e_{\rm gw}$ is measured. Because eccentricity induces modulations in the instantaneous frequency ω_{22}, we obtain a monotonic orbit-averaged $\langle\omega_{22}\rangle$ by taking the orbital average of the instantaneous ω_{22} (see Sec. II. E. 2 of [57] for more details). Between any two consecutive extrema [local maxima (pericenters, $t^{\rm p}$) or minima (apocenters, $t^{\rm a}$) in the instantaneous ω_{22}] $t_i^{\rm X}$ and $t_{i+1}^{\rm X}$ one can define

$$\langle \omega_{22} \rangle_i^{\mathrm{X}} = \frac{1}{t_{i+1}^{\mathrm{X}} - t_i^{\mathrm{X}}} \int_{t_i^{\mathrm{X}}}^{t_{i+1}^{\mathrm{X}}} \omega_{22}(t) \mathrm{d}t = \frac{\phi_{22}(t_{i+1}^{\mathrm{X}}) - \phi_{22}(t_i^{\mathrm{X}})}{t_{i+1}^{\mathrm{X}} - t_i^{\mathrm{X}}}, \tag{12}$$

and associate $\langle \omega_{22} \rangle_i^{\mathrm{X}}$ with the midpoint between t_i^{X} and t_{i+1}^{X}:

$$\langle t \rangle_i^{X} = \frac{1}{2}(t_i^{\mathrm{X}} + t_{i+1}^{\mathrm{X}}). \tag{13}$$

Applying this procedure to all consecutive pairs of pericenter times, one can obtain the set $\{(\langle t \rangle_i^{\mathrm{p}}, \langle \omega_{22} \rangle_i^{\mathrm{p}})\}$ and similarly, the set $\{(\langle t \rangle_i^{\mathrm{a}}, \langle \omega_{22} \rangle_i^{\mathrm{a}})\}$ for apocenter times. Finally, taking the union of these two datasets, one can build an interpolant in time to obtain $\langle \omega_{22} \rangle(t)$ and use $\langle f_{\mathrm{ref}} \rangle(t_{\mathrm{ref}}) \equiv \langle \omega_{22} \rangle(t_{\mathrm{ref}})/(2\pi)$ for defining the reference frequency $\langle f_{\mathrm{ref}} \rangle$ corresponding to a reference time t_{ref}.

Presenting our results with a standardized definition facilitates one-to-one comparisons with similar studies in the past and enables future studies to do the same with the results in this work.

D. Parameter estimation setup

We obtain our results by performing Bayesian parameter inference runs using a state-of-the-art GW parameter inference framework built in `Bilby` [68] with a dynamical nested sampler `dynesty` [69]. For the injection and recovery, we use the publicly available eccentric waveform model `TEOBResumS-Dalí` [55,56,70–74].[6] In the following, we will denote the eccentricity that the waveform model takes as an input by e_{eob} and the frequency where e_{eob} is defined by f_{ref}. Additionally, we provide $\{\langle f_{\mathrm{ref}} \rangle, e_{\mathrm{gw}}\}$ for each injection to facilitate better comparisons across waveform models and systematics studies.[7] For a given model eccentricity e_{eob} at a model reference frequency f_{ref}, the standardized eccentricity e_{gw} at $\langle f_{\mathrm{ref}} \rangle$ is obtained by first generating the eccentric waveform modes for the given pair $\{f_{\mathrm{ref}}, e_{\mathrm{eob}}\}$ and then following the steps discussed in Sec. II C.

Ideally, to accurately describe an eccentric orbit, the waveform model should also include mean anomaly as a free parameter [57,58,64]. In this work, we use the version of `TEOBResumS-Dalí` that was used in Ref. [66] by the waveform developers to showcase the accuracy and robustness of their model. This version of `TEOBResumS-Dalí` does not allow mean anomaly as a free parameter. Although the most recent version of `TEOBResumS-Dalí`, released after the completion of this work, allows mean anomaly as a free parameter, this version is yet to be tested (at the time of this writing) in a parameter inference study by sampling over mean anomaly and is currently under review. Eccentric waveform models `Ecc1dSur` [64] and `SEOBNRv4EHM` [65,75] include mean anomaly as a free parameter, but these are not publicly available. Publicly available eccentric waveform models `SEOBNRE` [76,77] and `EccentricTD` [78] do not include mean anomaly as a free parameter but instead start at the pericenter or apocenter.[8]

Because the version of `TEOBResumS-Dalí` used in the work does not allow sampling over mean anomaly, Ref. [66] sampled over the reference frequency, i.e., the PE was performed by sampling over eccentricity and reference frequency with fixed mean anomaly. The motivation behind such an approach is that by varying the reference frequency with fixed mean anomaly one can expect to explore the same parameter space as in the case of varying mean anomaly at a fixed reference frequency. For example, in a recent work in Ref. [81], it was shown that one can map an eccentric NR waveform to an eccentric effective one-body waveform using just the initial eccentricity and reference frequency at the first apocenter (that is, at a fixed mean anomaly). Although sampling over reference frequency may reduce bias in PE compared to a fixed reference frequency when mean anomaly is fixed, no significant bias was found in the recovered parameters when sampling exclusively over eccentricity with both mean anomaly and reference frequency fixed (see Fig. 3. in Ref. [66]).

Contrary to Refs. [66,81] which suggest that using (eccentricity, mean anomaly) at fixed reference frequency and using (eccentricity, reference frequency) at fixed mean anomaly are equivalent, it has been also argued that sampling over eccentricity and reference frequency with fixed mean anomaly may not be equivalent to sampling over eccentricity and mean anomaly with fixed reference frequency (see the introduction in Ref. [82]) since these two methods may not explore the same parameter space. In addition, varying reference frequency changes the reference point where binary properties are measured.

Given the fact that no significant bias was reported by the waveform developers in Ref. [66] when sampling only eccentricity with fixed reference frequency and that this version does not allow varying mean anomaly, we restrict our PE to sample only over eccentricity. However, future works that will use the recent version of `TEOBResumS-Dalí` once it is reviewed, should sample over mean

---

[6] We use the commit 0f19532 of the eccentric branch of `TEOBResumS` available at https://bitbucket.org/eob_ihes/teobresums/.

[7] Note that we sample over the model eccentricity e_{eob} and not e_{gw}.

[8] In some classes of GW sources, eccentricity and mean anomaly may not be sufficient to describe the orbit. For example, in Ref. [79], the Arnowitt-Deser-Misner energy and angular momentum are used to describe a generic planar orbit. See also Ref. [80] which uses the same parametrization to study the possibility of GW190521 resulting from a dynamical capture of two nonspinning black holes.

anomaly to reduce any potential bias due to neglecting mean anomaly.

To obtain the 2D posteriors on $\Delta M_f/\bar{M}_f$ and $\Delta\chi_f/\bar{\chi}_f$ for the IMRCT, we use the `summarytgr` command line tool from `PESummary` [83]. It provides the posteriors on $\Delta M_f/\bar{M}_f$ and $\Delta\chi_f/\bar{\chi}_f$ in a postprocessing step making use of mass and spin posterior samples along with the NR fits for the final mass and the final spin parameters. The uninformative priors used for the mass and spin parameters forces nontrivial undesirable priors on $\Delta M_f/\bar{M}_f$ and $\Delta\chi_f/\bar{\chi}_f$ obtained in the postprocessing. To revoke this effect and to impose agnostic priors on these inference parameters used to probe GR violation, we reweight[9] the 2D posterior to a flat prior on the deviation parameters, as is routinely done by the LVK [11,85].

Given the posterior samples obtained in the PE from the inspiral and postinspiral part, `summarytgr` uses an NR informed fit to obtain the final mass and spin posteriors. This fit is based on quasicircular NR simulations only and does not take into account any eccentric corrections which has been shown to be negligible at the quasi-Newtonian level with small eccentricity approximation [53]. Currently, we lack a sufficient number of NR simulations of merging eccentric binaries required for obtaining the eccentricity corrected NR fit for final mass and final spin. We measure $\{\langle f_{\rm ref}\rangle, e_{\rm gw}\}$ for a given $\{f_{\rm ref}, e_{\rm eob}\}$ using `gw_eccentricity` [57].

III. RESULTS

The main result of this work can be divided into two parts. The first part, Sec. III A, discusses the effect of neglecting eccentricity in the waveform template on the IMRCT. The second part, Sec. III B, demonstrates the robustness of the IMRCT performed on GW data containing an eccentric signal using a waveform template that includes physics required to describe GWs coming from binaries on an eccentric orbit. We list the injection values and priors in Table I and summarize the results of the study of bias in IMRCT due to neglecting eccentricity in Table II.

A. Effects of neglecting eccentricity in templates on IMRCT

1. Aligned spin case

First, we focus on studying the cases where the spins of the binary components are aligned with the orbital angular momentum of the binary. It is convenient to define the tilts $\theta_i^{\mathbf{SL}}$ as the angle between of the component spin $\mathbf{S}_i$ and the orbital angular momentum $\mathbf{L}$:

TABLE I. Injection values of the binary parameters and corresponding priors used for PE with `Bilby` [68]. $\mathcal{U}(a,b)$ stands for uniform prior in the range (a,b). $\sin(0,\pi)$ and $\cos(-\pi/2,\pi/2)$ stand for the sine and cosine priors, respectively on the ranges mentioned. Single values represent Dirac delta priors peaked at those values. Different values in the curly braces represent different injections. The table, therefore, represents 12 injections—six different eccentricities each with two different spin configurations.

Parameter	Injected value	Prior
$\mathcal{M}_c(M_\odot)$	26.36	$\mathcal{U}(12,45)$
q	0.8	$\mathcal{U}(0.25,1)$
χ_1	$\{0.2,0.4\}$	$\mathcal{U}(0,0.99)$
χ_2	$\{0.1,0.3\}$	$\mathcal{U}(0,0.99)$
$\theta_1^{\mathbf{SL}}$ (rad)	0	0
$\theta_2^{\mathbf{SL}}$ (rad)	0	0
d_L(MPc)	410	$\mathcal{U}(50,2000)$
ι	0.78	$\sin(0,\pi)$
α(rad)	4.89	$\mathcal{U}(0,2\pi)$
δ	−0.218	$\cos(-\pi/2,\pi/2)$
ψ(rad)	0.54	$\mathcal{U}(0,\pi)$
t_c(s)	$1126259462(\equiv t_0)$	$\mathcal{U}(t_0-2,t_0+2)$
ϕ_c(rad)	4.205	$\mathcal{U}(0,2\pi)$
$e_{\rm eob}$	$\{0.05,0.06,0.07,0.08,0.09,0.10\}$	10^{-4}
$f_{\rm ref}$(Hz)	20	20

$$\theta_i^{\mathbf{SL}} = \cos^{-1}\left(\frac{\mathbf{L}.\mathbf{S}_i}{|\mathbf{L}||\mathbf{S}_i|}\right) \qquad i=\{1,2\}. \tag{14}$$

Since `TEOBResumS-Dalí` can describe only nonprecessing systems, $\theta_i^{\mathbf{SL}}$ can take only two values 0 (aligned) or π (antialigned). In this section, we consider binary systems with $\theta_{1,2}^{\mathbf{SL}}=0$. Since the waveform model only allows tilts of either 0 or π, and does not allow sampling over arbitrary spin orientations, we choose the prior on the tilts to be a Dirac delta function peaked at the injection value.

We choose the component masses to be similar to that of the gravitational wave event GW150914. For this study we choose a total mass of system that lies within the "golden mass" range $M\in[50-100]M_\odot$ which ensures high enough SNRs both in the inspiral and postinspiral parts of the signal [23]. The injection parameters and the priors are noted in Table I. The injection eccentricities $e_{\rm eob}\in\{0.05,0.06,0.07,0.08,0.09,0.1\}$ are defined at a reference frequency of $f_{\rm ref}=20$ Hz. These injected waveforms have $e_{\rm gw}$ values $\{0.040,0.048,0.055,0.063,0.071,0.079\}$[10] measured at an orbit-averaged frequency of $\langle f_{\rm ref}\rangle=25$ Hz. To understand the effect of spin magnitudes on IMRCT systematics, we consider two

---

[9] Reweighting of posterior refers to removing the effect of any nontrivial undesirable prior on the posterior (see Chapter 5 in Ref. [84] for details). This is done when there is no prior information about the parameter in consideration or the prior information about the parameter is unphysical and one wants to be as objective as possible.

[10] We used the `ResidualAmplitude` method within `gw_eccentricity` to measure these eccentricities.

TABLE II. Summary of the study of bias in IMRCT due to neglecting eccentricity. It provides the threshold injection eccentricity (e_{eob} at 20 Hz) at or above which the IMRCT result is biased at 68% and 90% confidence. It also provides the eccentricity e_{gw} in terms of standardized definition [57] at an orbital averaged frequency $\langle f_{\mathrm{ref}} \rangle = 25$ Hz corresponding to each of these threshold injections. As an example, for an aligned low spin $(\chi_1, \chi_2) = (0.2, 1.0)$ system, GR is excluded at 68% confidence for $e_{\mathrm{eob}} = 0.05$ ($e_{\mathrm{gw}} = 0.04$), and GR is excluded at 90% confidence for $e_{\mathrm{eob}} = 0.07$ ($e_{\mathrm{gw}} = 0.055$).

Dimensionless component spins	Tilts	Threshold eccentricity for GR violation at 90%		Threshold eccentricity for GR violation 68%	
(χ_1, χ_2)	$(\theta_1^{\mathrm{SL}}, \theta_2^{\mathrm{SL}})$	e_{eob} at $f_{\mathrm{ref}} = 20$ Hz	e_{gw} at $\langle f_{\mathrm{ref}} \rangle = 25$ Hz	e_{eob} at $f_{\mathrm{ref}} = 20$ Hz	e_{gw} at $\langle f_{\mathrm{ref}} \rangle = 25$ Hz
(0.4, 0.3)	(0, 0)			0.09	0.071
(0.2, 0.1)	(0, 0)	0.07	0.055	0.05	0.040
(0.4, 0.3)	$(\pi, 0)$			0.07	0.056
(0.4, 0.3)	$(0, \pi)$	0.10	0.079	0.09	0.071
(0.4, 0.3)	(π, π)			0.08	0.064

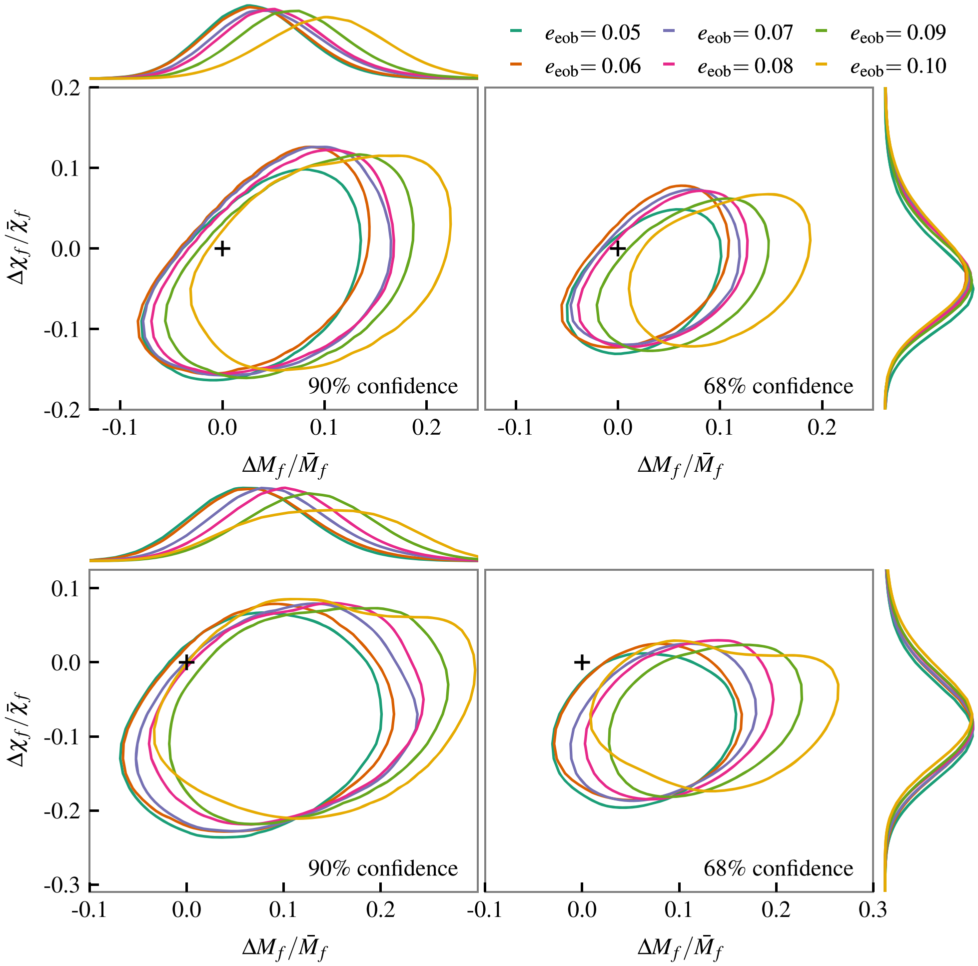

FIG. 1. Bias in IMRCT due to neglecting eccentricity in recovery template. The top and the bottom row represent the IMRCT result for the aligned spin configurations with dimensionless component spins $(\chi_1, \chi_2) = (0.4, 0.3)$ and $(\chi_1, \chi_2) = (0.2, 0.1)$, respectively. The contours represent the joint probability distribution of the final mass deviation $\Delta M_f/\bar{M}_f$ and final spin deviation $\Delta\chi_f/\bar{\chi}_f$ at 90% and 68% confidence on the left and the right panels, respectively. For $(\chi_1, \chi_2) = (0.4, 0.3)$, the GR value is excluded at 68% confidence at $e_{\mathrm{eob}} = 0.09$. For $(\chi_1, \chi_2) = (0.2, 0.1)$, the GR value is excluded at 68% and 90% confidence for $e_{\mathrm{eob}} = 0.05$ and 0.07, respectively.

different choices of dimensionless component spins, one low $(\chi_1, \chi_2) = (0.2, 0.1)$ and one moderate $(\chi_1, \chi_2) = (0.4, 0.3)$, for the set of injected eccentricities. All the injections considered in this study have Hanford-Livingston-Virgo network (at O4 design sensitivity) SNR in the range 27–52.

While recovering the injection, we use a Dirac delta prior on eccentricity peaked at $e_{\rm eob} = 10^{-4}$ making the parameter estimation procedure equivalent to one using a quasicircular template.[11]

The results of these IMRCTs are shown in Fig. 1. The top row shows the results for $(\chi_1, \chi_2) = (0.4, 0.3)$, and the bottom row shows the same for $(\chi_1, \chi_2) = (0.2, 0.1)$. In each of these rows, the left panel shows the isoprobability contours of the 2D probability distribution on the final mass deviation $\Delta M_f/\bar{M}_f$ (along x axis) and the final spin deviation $\Delta\chi_f/\bar{\chi}_f$ (along y axis) plane at 90% confidence. The right panel shows the same at 68% confidence. Different contours in each panel correspond to the injected eccentricities $e_{\rm eob} \in \{0.05, 0.06, 0.07, 0.08, 0.09, 0.1\}$ as noted on the top of the right panel. Figure 1 also shows the marginalized 1D posterior of $\Delta M_f/\bar{M}_f$ on top of the left panel and that of $\Delta\chi_f/\bar{\chi}_f$ on the right of the right panel.

It can be noted that in the case of moderate spin $(\chi_1, \chi_2) = (0.4, 0.3)$, for smaller eccentricities ($e_{\rm eob} < 0.08$), the contours at 90% and 68% contain the point (0, 0) denoted by $+$ which stands for zero-deviation from GR. We will denote this point of zero deviation from GR as the "GR value." However, for larger eccentricities ($e_{\rm eob} \gtrsim 0.08$), the contours are shifted toward positive deviation in $\Delta M_f/\bar{M}_f$, and the GR value is excluded at 68% confidence for $e_{\rm eob} \geq 0.09$. For smaller spins $(\chi_1, \chi_2) = (0.2, 1)$, the bias is more severe. For the low spin case (bottom row in Fig. 1), the GR value is excluded at 68% confidence for $e_{\rm eob} = 0.05$ and at 90% confidence for $e_{\rm eob} = 0.07$.

One can also construct a statistical measure of the deviation from GR using the GR quantile $Q_{\rm GR}$ which is the fraction of the posterior samples contained within the isoprobability contour that passes through the GR value [no-deviation point (0,0)]. A smaller $Q_{\rm GR}$ implies a better agreement with GR since the GR value is contained within a smaller isoprobability contour. In this work, we compute the GR quantile in a slightly different way. Instead of using the samples directly, we use an interpolated histogram of the 2D probability distribution. In particular, we use the implementation in `summarytgr` within `PESummary` [83].

In Fig. 2, we plot the $Q_{\rm GR}$ for different component spin configurations as a function of the injection eccentricities. It shows the overall trend of $Q_{\rm GR}$ increasing with $e_{\rm eob}$. While for moderate spins $(\chi_1, \chi_2) = (0.4, 0.3)$, $Q_{\rm GR}$ becomes ≈68% at $e_{\rm eob} = 0.08$, for low spins $(\chi_1, \chi_2) = (0.2, 0.1)$, $Q_{\rm GR}$ becomes $> 68\%$ at $e_{\rm eob} = 0.05$ and $\gtrsim 90\%$ at $e_{\rm eob} = 0.07$.

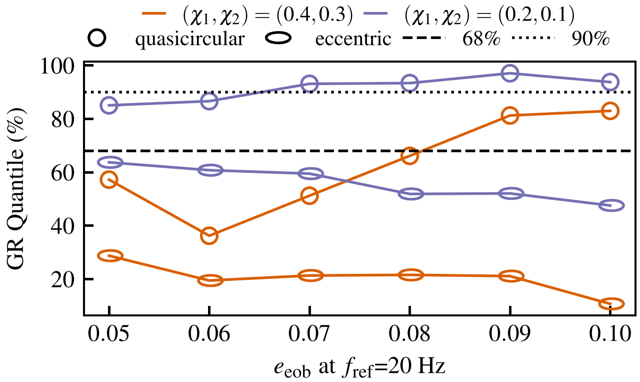

FIG. 2. GR Quantile $Q_{\rm GR}$ vs injected eccentricity for different component spins for the aligned spin systems. Small $Q_{\rm GR}$ indicates better agreement with GR. Circles denote the quasicircular recovery, and the ellipses denote the eccentric recovery. The low spin $(\chi_1, \chi_2) = (0.2, 0.1)$ and moderate spin $(\chi_1, \chi_2) = (0.4, 0.3)$ case are denoted by violet and orange, respectively. When recovered with quasicircular templates, low spin cases show more bias compared to the moderate spin case.

2. Antialigned spin case

In this section, we study how the bias in the IMRCT due to neglecting eccentricity in the recovery waveform model depends on the orientation of the spin with respect to the angular momentum of the system. Let the pair $(\theta_1^{\bf SL}, \theta_2^{\bf SL})$ denote the tilts of the spin $\mathbf{S}_1$ of the primary and the spin $\mathbf{S}_2$ of the secondary, respectively, with respect to the orbital angular momentum $\mathbf{L}$ of the system. We consider the following three cases:

1. $(\pi, 0)$: $\mathbf{S}_1$ is antialigned and $\mathbf{S}_2$ is aligned.
2. $(0, \pi)$: $\mathbf{S}_1$ is aligned and $\mathbf{S}_2$ is antialigned.
3. (π, π): Both $\mathbf{S}_1$ and $\mathbf{S}_2$ are antialigned.

We consider only the moderate spin case where the dimensionless spins are (0.4, 0.3). The other parameters remain the same as in Table I. We use a Dirac delta prior peaked at the injected values for the tilts. The number of injections for each of these tilts is six for six different eccentricities making a total of 18 injections for these three tilt configurations.

The rows from the top to bottom in Fig. 3 show the IMRCT results for the cases of primary antialigned, secondary antialigned, and both antialigned, respectively. In each of these figures, the left panel shows the isoprobability contours at 90% confidence, and the right panel shows the same at 68% confidence in the $\Delta M_f/\bar{M}_f - \Delta\chi_f/\bar{\chi}_f$ plane. The general trend is similar to that of aligned spin cases in Sec. III A 1.

---

[11] For $e_{\rm eob} \leq 10^{-4}$, the corresponding $e_{\rm gw}$ is 10^{-6} implying the waveforms to be essentially quasicircular. See Fig. 10 in [57].

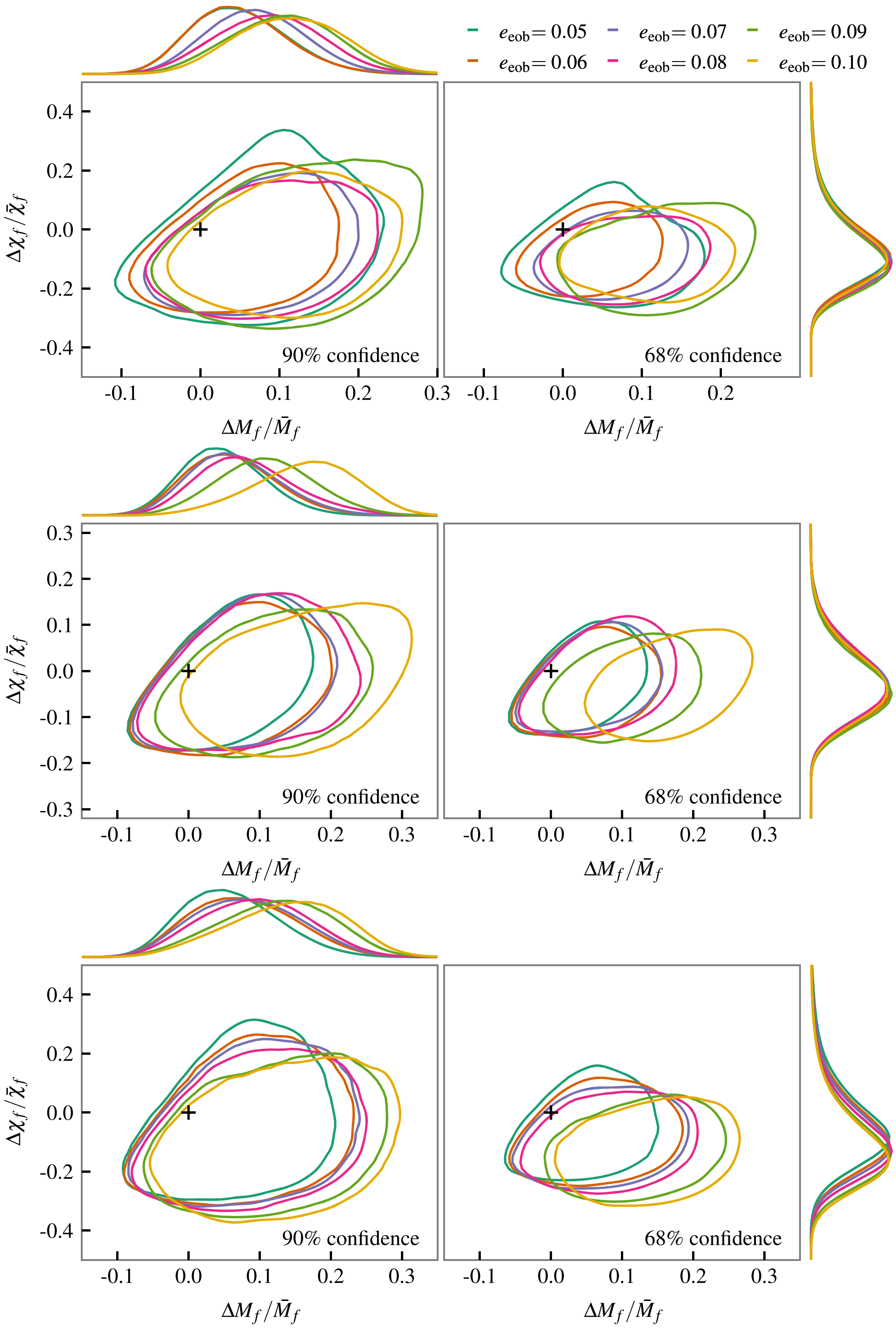

FIG. 3. IMRCT with quasicircular recovery template for injections with antialigned spin configurations.The panels from the top to bottom correspond to primary antialigned, secondary antialigned, and both antialigned spin configurations, respectively. For all three cases, the dimensionless component spin magnitudes are $(\chi_1, \chi_2) = (0.4, 0.3)$. Owing to neglecting eccentricity in the recovery template, the GR value is excluded at 68% confidence at $e_{\rm eob} = 0.07$, 0.09 and 0.08 for primary antialigned, secondary antialigned, and both antialigned cases, respectively. The GR value is also excluded at 90% confidence for secondary antialigned at $e_{\rm eob} = 0.1$.

TABLE III. Injection values of the eccentricities and priors for IMRCTs with eccentric recovery.

Parameter	Injected value	Prior
e_{eob}	$\{0.05, 0.06, 0.07, 0.08, 0.09, 0.10\}$	$\mathcal{U}(8\times 10^{-3}, 0.15)$
$f_{\mathrm{ref}}(\mathrm{Hz})$	20	20

B. IMRCT with eccentric signal

In the previous section, we showed that IMRCT shows spurious deviation from GR when the parameters from an eccentric gravitational wave signal are inferred using a quasicircular waveform model (using a delta function prior on eccentricity fixed at $e_{\mathrm{eob}} = 10^{-4}$). In this section, we show that such spurious deviations go away when the eccentric waveform model is used instead of the quasicircular model by allowing the sampler to sample from a uniform prior on eccentricity as described in Table III.

1. Aligned spin case

First, we consider the case of aligned spin where both the primary and the secondary spin are aligned with the angular momentum of the system, i.e., $\theta^{\mathbf{SL}}_{1,2} = 0$. In Fig. 4, we show the results of IMRCTs with a set of eccentric aligned spin signals. The top row shows the result for injections with moderate component spins $(\chi_1, \chi_2) = (0.4, 0.3)$, and the bottom row shows the result for low component spins $(\chi_1, \chi_2) = (0.2, 0.1)$. The set of injected eccentricities and the prior on the eccentricity for both of these spin configurations are provided in Table III. The other parameters remain the same as in Sec. III A 1.

In each row of Fig. 4, the left (right) panel shows the isoprobability contours of the 2D probability distribution in the $\Delta M_f/\bar{M}_f - \Delta\chi_f/\bar{\chi}_f$ plane at 90% (68%) confidence. The 1D posterior on $\Delta M_f/\bar{M}_f$ is shown on the top of the left panel, and the 1D posterior on $\Delta\chi_f/\bar{\chi}_f$ is shown on the

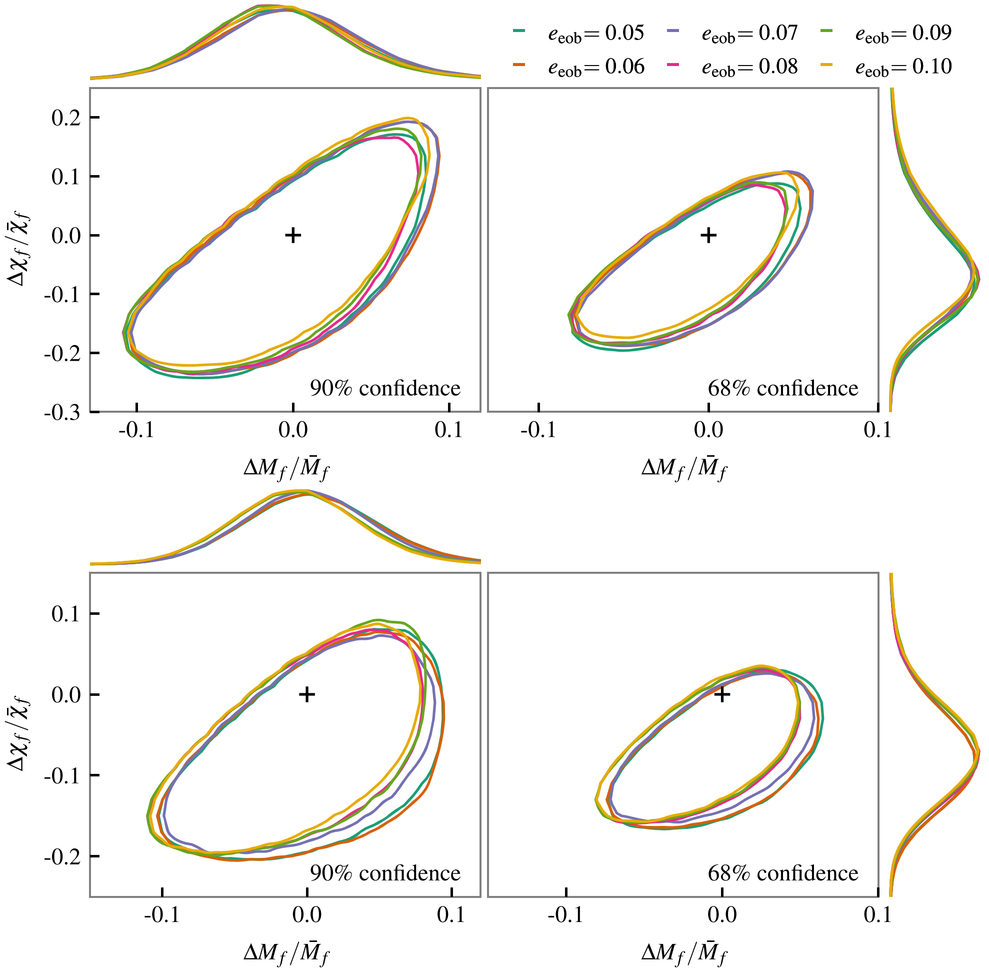

FIG. 4. IMRCT with eccentric recovery template for aligned spin injections. The top row corresponds to $(\chi_1, \chi_2) = (0.4, 0.3)$, and the bottom row corresponds to $(\chi_1, \chi_2) = (0.2, 0.1)$. Same as Fig. 1, but now the injections are recovered with eccentric templates instead of quasicircular templates. GR value is included within the isoprobability contours at both the 68% and 90% confidence levels for all injections for these two spin configurations.

right of the right plot. In both of these spin configurations, for all the injected eccentricities, we find IMRCTs to be unbiased both at 68% and 90% confidence.

For these two aligned spin configurations, the GR quantile $Q_{\rm GR}$, when recovered with an eccentric waveform template, is shown using ellipses in Fig. 2. $Q_{\rm GR}$ is plotted as a function of the injection eccentricities. It can be seen that for all the injected eccentricities, the $Q_{\rm GR}$ remains $< 68\%$ for low spins $(\chi_1, \chi_2) = (0.2, 0.1)$ and $< 30\%$ for moderate spins $(\chi_1, \chi_2) = (0.4, 0.3)$ implying an agreement with GR.

2. Antialigned spin case

We now turn our focus to the potential effects of the orientation of the component spins on IMRCTs with eccentric signal when recovered with eccentric waveform models. We consider the same injections as in Sec. III A 2; we consider three possible configurations where the pair of tilts may take the values $(\pi, 0), (0, \pi)$ or (π, π) with the component dimensionless spins $(\chi_1, \chi_2) = (0.4, 0.3)$. In Sec. III A 2, these injections were recovered using a quasicircular template which resulted in spurious bias in the IMRCT result. Now we recover these injections with eccentric template using a prior on eccentricity as shown in Table III.

The rows from the top to bottom in Fig. 5 show the IMRCT contours for primary antialigned, secondary antialigned, and both antialigned configurations, respectively. For a given row, the left (right) panel shows the isoprobability contours of the 2D probability distribution in the $\Delta M_f/\bar{M}_f - \Delta\chi_f/\bar{\chi}_f$ plane at 90% (68%) confidence. The 1D posterior on $\Delta M_f/\bar{M}_f$ is shown on top of the left panel, and the 1D posterior on $\Delta\chi_f/\bar{\chi}_f$ is shown on the right of the right panel. Different contours in each panel correspond to different injected eccentricity as denoted on top of the right panel of each row. Unlike the results in Fig. 3, all the contours in Fig. 5 include the GR value.

We also plot the $Q_{\rm GR}$ (denoted by ellipses) values of the IMRCTs corresponding to these injections in Fig. 6. Note that the $Q_{\rm GR}$ values for these cases of recovery with eccentric templates are very small compared to the quasicircular recovery (denoted by circles). The $Q_{\rm GR}$ for eccentric recovery is $< 68\%$ for all considered eccentricities in these three antialigned spin configurations. While for the primary antialigned cases, the $Q_{\rm GR}$ remains $\lesssim 10\%$, for the secondary antialigned and both antialigned cases, the GR quantile is even smaller, $Q_{\rm GR} \lesssim 5\%$ implying excellent agreement with GR.

IV. SUMMARY AND OUTLOOK

The IMRCT [23,24] is one among several tests of GR with GWs used by the LVK. While model agnostic in the sense that it is not based on any particular alternative theory of gravity, it does nevertheless crucially rely on the CBC template waveform being an accurate representation of the GW signal. Thus, intuitively, one would expect spurious violations of this test when physical and environmental effects are not accounted for in the waveform model.

To demonstrate this, in this work, we focus our attention on GWs from eccentric compact binaries. We inject, in zero noise assuming an O4-like noise PSD, synthetic GW150914-like CBC signals but with a range of residual eccentricities at a reference frequency of $f_{\rm ref} = 20$ Hz. The spins are always assumed to lie along the orbital angular momentum (z-) axis, although we consider two different sets of spin magnitudes, and all possible orientation(aligned/antialigned) combinations of the binary components along the z axis. We then perform the IMRCT with quasicircular templates (these being routinely used by current implementations of the IMRCT), as well as eccentric templates.

We find that, as expected, the IMRCT gets progressively biased with increasing injected eccentricity while recovering with quasicircular templates. At 68% confidence, we find that the IMRCT starts to get violated for eccentricities—as defined by the waveform model used—between $e_{\rm eob} \sim 0.05$–0.09 at a reference frequency $f_{\rm ref} = 20$ Hz, for our chosen CBC systems. Converting this to a standardized definition of eccentricity [57], these values become $e_{\rm gw} \sim 0.04$–0.07 at an orbital averaged frequency $\langle f_{\rm ref} \rangle = 25$ Hz. Indeed, as the eccentricity is increased, the violations occur even at 90% confidence.

On the other hand, when recovering with eccentric templates, we find that the IMRCT is *always* satisfied, regardless of the spin magnitude, orientation, or eccentricity value, at 68% confidence. Our work therefore demonstrates the need for accurate eccentric waveform models for IMRCT and possibly other tests of GR. Moreover, our work complements and expands on previous work studying the effect of neglect of eccentricity on the IMRCT. These either use approximate GW PE likelihoods [53], or only study the potential bias in the IMRCT caused by recovering a few eccentric numerical relativity waveforms with phenomenological waveforms [54].

Two important limitations of our work must be pointed out. The first is that the injections are performed in zero noise rather than real noise. This could potentially introduce additional fluctuations in the IMRCT as a consequence of a particular noise realization. The second is that the recovery of the IMRCT has been tested using identical injection and recovery waveform models. It would be of interest to consider eccentric numerical-relativity injections recovered with other eccentric waveform models that are nominally used for GW PE. Such a study might potentially demonstrate nontrivial biases in the IMRCT even when eccentric waveforms are used, and if not, would ascertain the feasibility of using current eccentric waveform models for tests of GR. We plan to address the said limitations in future work.

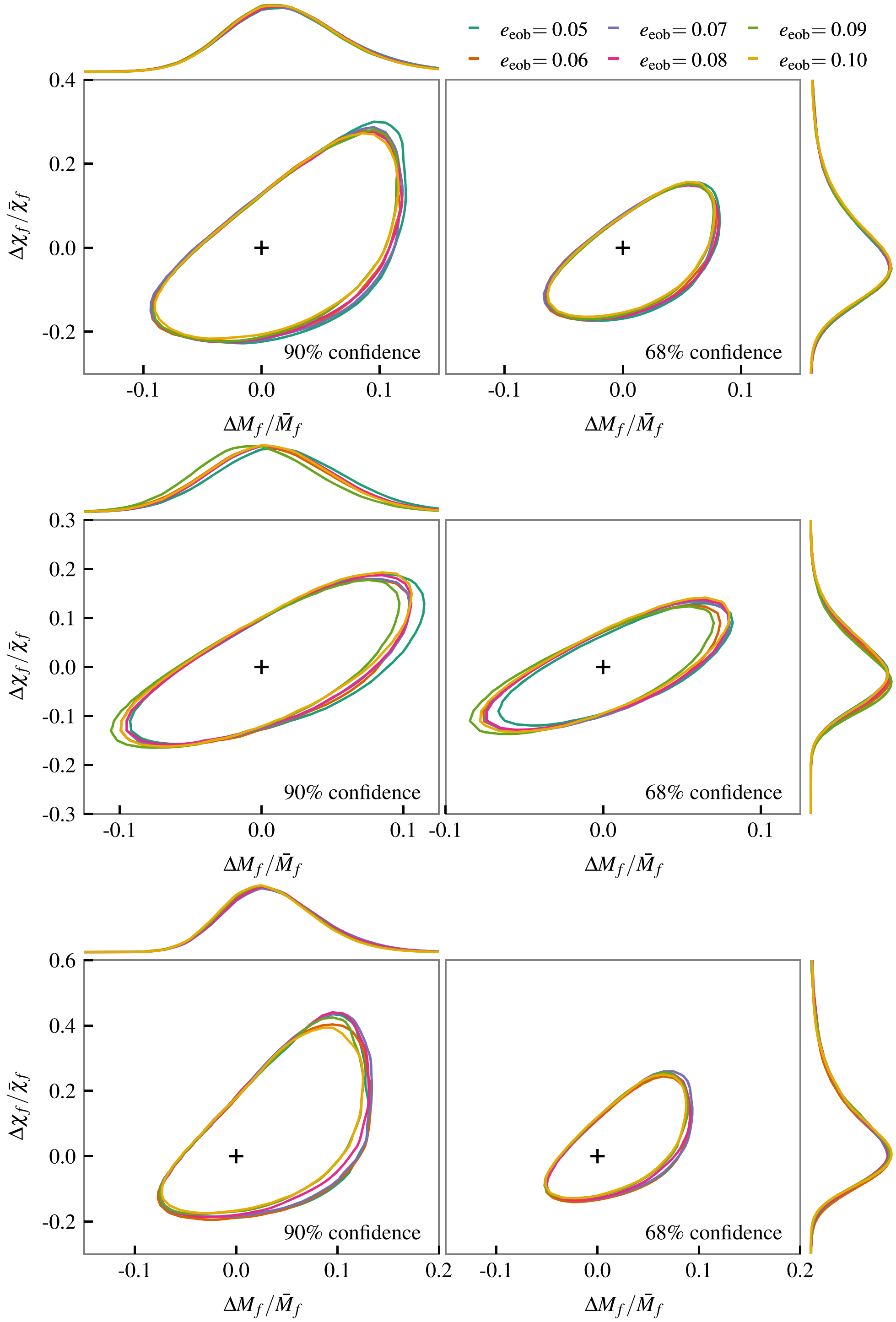

FIG. 5. IMRCT with eccentric recovery template for injections with antialigned spin configurations. The rows from the top to bottom correspond to primary antialigned, secondary antialigned, and both antialigned spin configurations, respectively. For all three cases, the dimensionless component spin magnitudes are $(\chi_1, \chi_2) = (0.4, 0.3)$. Same as Fig. 3 but now the injections are recovered with eccentric templates instead of quasicircular templates. Note that the GR value is included at both 68% and 90% confidence for all the injections for these three configurations.

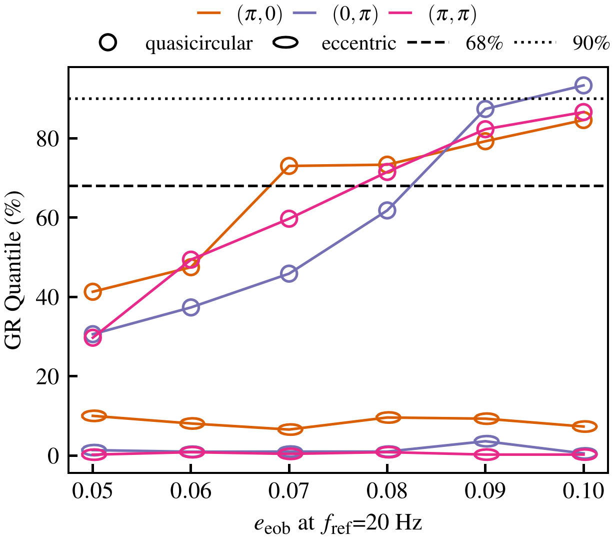

FIG. 6. GR Quantile $Q_{\rm GR}$ vs injected eccentricity for different component spin alignments for $(\chi_1, \chi_2) = (0.4, 0.3)$. Small $Q_{\rm GR}$ indicates better agreement with GR. Circles denote the quasicircular recovery, and the ellipses denote the eccentric recovery. When recovered with quasicircular template, the $Q_{\rm GR}$ tend to increase with increasing eccentricity implying increasing bias in IMRCT due to neglecting eccentricity in the waveform model. On the other hand, for eccentric recovery, the $Q_{\rm GR}$ remains within 68% for all eccentricities. For all cases of eccentric recovery, the $Q_{\rm GR}$ is $\lesssim$10%. In the secondary antialigned and both antialigned cases, the $Q_{\rm GR}$ becomes even smaller ($< 5\%$) implying excellent agreement with GR.

ACKNOWLEDGMENTS

We thank the anonymous referees for their useful comments and suggestions. We thank Pankaj Saini for a careful reading of the draft. We also thank Prayush Kumar, Nathan K. Johnson-McDaniel, Aditya Vijaykumar, and members of the ICTS-TIFR Astrophysical Relativity Group for useful discussions. M. A. S.'s research was supported by the Department of Atomic Energy, Government of India under Project No. RTI4001 and the National Research Foundation of Korea under Grant No. NRF-2021R1A2C2012473. S. A. B. acknowledges support from the Department of Science and Technology and the Science and Engineering Research Board (SERB) of India via Swarnajayanti Fellowship Grant No. DST/SJF/PSA-01/2017-18 and support from Infosys Foundation. The authors are grateful for computational resources provided by the LIGO Laboratory and supported by National Science Foundation Grants No. PHY-0757058 and No. PHY-0823459. The authors also acknowledge the use of the Alice cluster at the International Centre for Theoretical Sciences.

[1] J. Aasi *et al.* (LIGO Scientific Collaboration), Advanced LIGO, Classical Quantum Gravity **32**, 074001 (2015).

[2] F. Acernese *et al.* (Virgo Collaboration), Advanced Virgo: A second-generation interferometric gravitational wave detector, Classical Quantum Gravity **32**, 024001 (2015).

[3] R. Abbott *et al.* (KAGRA, Virgo, and LIGO Scientific Collaborations), GWTC-3: Compact binary coalescences observed by LIGO and Virgo during the second part of the third observing run, Phys. Rev. X **13**, 041039 (2023).

[4] Benjamin P. Abbott *et al.* (LIGO Scientific and Virgo Collaborations), GW170817: Observation of gravitational waves from a binary neutron star inspiral, Phys. Rev. Lett. **119**, 161101 (2017).

[5] B. P. Abbott *et al.* (LIGO Scientific and Virgo Collaborations), GW190425: Observation of a compact binary coalescence with total mass $\sim 3.4 M_\odot$, Astrophys. J. Lett. **892**, L3 (2020).

[6] R. Abbott *et al.* (LIGO Scientific, KAGRA, and Virgo Collaborations), Observation of gravitational waves from two neutron star–black hole coalescences, Astrophys. J. Lett. **915**, L5 (2021).

[7] B. S. Sathyaprakash and B. F. Schutz, Physics, astrophysics and cosmology with gravitational waves, Living Rev. Relativity **12**, 2 (2009).

[8] Kazunori Akiyama *et al.* (Event Horizon Telescope Collaboration), First M87 Event Horizon Telescope results.

I. The shadow of the supermassive black hole, Astrophys. J. Lett. **875**, L1 (2019).

[9] Dimitrios Psaltis, Testing general relativity with the Event Horizon Telescope, Gen. Relativ. Gravit. **51**, 137 (2019).

[10] T. Akutsu *et al.* (KAGRA Collaboration), Overview of KAGRA: Detector design and construction history, Prog. Theor. Exp. Phys. **2021**, 05A101 (2021).

[11] R. Abbott *et al.* (LIGO Scientific, Virgo, and KAGRA Collaborations), Tests of general relativity with GWTC-3, arXiv:2112.06861.

[12] B. P. Abbott *et al.* (LIGO Scientific and Virgo Collaborations), Tests of general relativity with GW150914, Phys. Rev. Lett. **116**, 221101 (2016); **121**, 129902(E) (2018).

[13] B. P. Abbott *et al.* (LIGO Scientific and Virgo Collaborations), Tests of general relativity with the binary black hole signals from the LIGO-Virgo catalog GWTC-1, Phys. Rev. D **100**, 104036 (2019).

[14] R. Abbott *et al.* (LIGO Scientific and Virgo Collaborations), Properties and astrophysical implications of the $150M_{\odot}$ binary black hole merger GW190521, Astrophys. J. Lett. **900**, L13 (2020).

[15] Luc Blanchet and B. S. Sathyaprakash, Detecting the tail effect in gravitational wave experiments, Phys. Rev. Lett. **74**, 1067 (1995).

[16] Luc Blanchet and Bangalore Suryanarayana Sathyaprakash, Signal analysis of gravitational wave tails, Classical Quantum Gravity **11**, 2807 (1994).

[17] K. G. Arun, Bala R. Iyer, M. S. S. Qusailah, and B. S. Sathyaprakash, Probing the non-linear structure of general relativity with black hole binaries, Phys. Rev. D **74**, 024006 (2006).

[18] K. G. Arun, Bala R. Iyer, M. S. S. Qusailah, and B. S. Sathyaprakash, Testing post-Newtonian theory with gravitational wave observations, Classical Quantum Gravity **23**, L37 (2006).

[19] Nicolas Yunes and Frans Pretorius, Fundamental theoretical bias in gravitational wave astrophysics and the parameterized post-Einsteinian framework, Phys. Rev. D **80**, 122003 (2009).

[20] Chandra Kant Mishra, K. G. Arun, Bala R. Iyer, and B. S. Sathyaprakash, Parametrized tests of post-Newtonian theory using Advanced LIGO and Einstein Telescope, Phys. Rev. D **82**, 064010 (2010).

[21] T. G. F. Li, W. Del Pozzo, S. Vitale, C. Van Den Broeck, M. Agathos, J. Veitch, K. Grover, T. Sidery, R. Sturani, and A. Vecchio, Towards a generic test of the strong field dynamics of general relativity using compact binary coalescence, Phys. Rev. D **85**, 082003 (2012).

[22] T. G. F. Li, W. Del Pozzo, S. Vitale, C. Van Den Broeck, M. Agathos, J. Veitch, K. Grover, T. Sidery, R. Sturani, and A. Vecchio, Towards a generic test of the strong field dynamics of general relativity using compact binary coalescence: Further investigations, J. Phys. Conf. Ser. **363**, 012028 (2012).

[23] Abhirup Ghosh *et al.*, Testing general relativity using golden black-hole binaries, Phys. Rev. D **94**, 021101 (2016).

[24] Abhirup Ghosh, Nathan K. Johnson-Mcdaniel, Archisman Ghosh, Chandra Kant Mishra, Parameswaran Ajith, Walter Del Pozzo, Christopher P. L. Berry, Alex B. Nielsen, and Lionel London, Testing general relativity using gravitational wave signals from the inspiral, merger and ringdown of binary black holes, Classical Quantum Gravity **35**, 014002 (2018).

[25] B. P. Abbott *et al.* (LIGO Scientific and Virgo Collaborations), Tests of general relativity with GW170817, Phys. Rev. Lett. **123**, 011102 (2019).

[26] Clifford M. Will, Bounding the mass of the graviton using gravitational wave observations of inspiralling compact binaries, Phys. Rev. D **57**, 2061 (1998).

[27] P. C. Peters and J. Mathews, Gravitational radiation from point masses in a Keplerian orbit, Phys. Rev. **131**, 435 (1963).

[28] P. C. Peters, Gravitational radiation and the motion of two point masses, Phys. Rev. **136**, B1224 (1964).

[29] A. G. Abac *et al.* (LIGO Scientific, Virgo, and KAGRA Collaborations), Search for eccentric black hole coalescences during the third observing run of LIGO and Virgo, arXiv:2308.03822.

[30] B. P. Abbott *et al.* (LIGO Scientific and Virgo Collaborations), Search for eccentric binary black hole mergers with Advanced LIGO and Advanced Virgo during their first and second observing runs, Astrophys. J. **883**, 149 (2019).

[31] Alexander H. Nitz, Amber Lenon, and Duncan A. Brown, Search for eccentric binary neutron star mergers in the first and second observing runs of Advanced LIGO, Astrophys. J. **890**, 1 (2019).

[32] Michela Mapelli, Binary black hole mergers: Formation and populations, Front. Astron. Space Sci. **7**, 38 (2020).

[33] Johan Samsing, Eccentric black hole mergers forming in globular clusters, Phys. Rev. D **97**, 103014 (2018).

[34] Michael Zevin, Johan Samsing, Carl Rodriguez, Carl-Johan Haster, and Enrico Ramirez-Ruiz, Eccentric black hole mergers in dense star clusters: The role of binary–binary encounters, Astrophys. J. **871**, 91 (2019).

[35] Isobel M. Romero-Shaw, Paul D. Lasky, and Eric Thrane, Four eccentric mergers increase the evidence that LIGO–Virgo–KAGRA's binary black holes form dynamically, Astrophys. J. **940**, 171 (2022).

[36] J. Samsing, I. Bartos, D. J. D'Orazio, Z. Haiman, B. Kocsis, N. W. C. Leigh, B. Liu, M. E. Pessah, and H. Tagawa, AGN as potential factories for eccentric black hole mergers, Nature (London) **603**, 237 (2022).

[37] Hiromichi Tagawa, Bence Kocsis, Zoltan Haiman, Imre Bartos, Kazuyuki Omukai, and Johan Samsing, Eccentric black hole mergers in active galactic nuclei, Astrophys. J. Lett. **907**, L20 (2021).

[38] Yoshihide Kozai, Secular perturbations of asteroids with high inclination and eccentricity, Astron. J. **67**, 591 (1962).

[39] M. L. Lidov, The evolution of orbits of artificial satellites of planets under the action of gravitational perturbations of external bodies, Planet. Space Sci. **9**, 719 (1962).

[40] Smadar Naoz, The eccentric Kozai-Lidov effect and its applications, Annu. Rev. Astron. Astrophys. **54**, 441 (2016).

[41] Fabio Antonini, Silvia Toonen, and Adrian S. Hamers, Binary black hole mergers from field triples: Properties, rates and the impact of stellar evolution, Astrophys. J. **841**, 77 (2017).

[42] Lisa Randall and Zhong-Zhi Xianyu, Induced ellipticity for inspiraling binary systems, Astrophys. J. **853**, 93 (2018).

[43] Hang Yu, Sizheng Ma, Matthew Giesler, and Yanbei Chen, Spin and eccentricity evolution in triple systems: From the Lidov-Kozai interaction to the final merger of the inner binary, Phys. Rev. D **102**, 123009 (2020).

[44] I. Bartos, S. Rosswog, V. Gayathri, M. C. Miller, D. Veske, and S. Marka, Hierarchical triples as early sources of *r*-process elements, arXiv:2302.10350.

[45] Pankaj Saini, Marc Favata, and K. G. Arun, Systematic bias on parametrized tests of general relativity due to neglect of orbital eccentricity, Phys. Rev. D **106**, 084031 (2022).

[46] Pankaj Saini, Sajad A. Bhat, Marc Favata, and K. G. Arun, Eccentricity-induced systematic error on parametrized tests of general relativity: Hierarchical Bayesian inference applied to a binary black hole population, Phys. Rev. D **109**, 084056 (2024).

[47] Marc Favata, Systematic parameter errors in inspiraling neutron star binaries, Phys. Rev. Lett. **112**, 101101 (2014).

[48] Marc Favata, Chunglee Kim, K. G. Arun, JeongCho Kim, and Hyung Won Lee, Constraining the orbital eccentricity of inspiralling compact binary systems with Advanced LIGO, Phys. Rev. D **105**, 023003 (2022).

[49] Eamonn O'Shea and Prayush Kumar, Correlations in gravitational-wave reconstructions from eccentric binaries: A case study with GW151226 and GW170608, Phys. Rev. D **108**, 104018 (2023).

[50] B. P. Abbott *et al.* (KAGRA, LIGO Scientific, and Virgo Collaborations), Prospects for observing and localizing gravitational-wave transients with Advanced LIGO, Advanced Virgo and KAGRA, Living Rev. Relativity **21**, 3 (2018).

[51] Curt Cutler and Eanna E. Flanagan, Gravitational waves from merging compact binaries: How accurately can one extract the binary's parameters from the inspiral wave form?, Phys. Rev. D **49**, 2658 (1994).

[52] Curt Cutler and Michele Vallisneri, LISA detections of massive black hole inspirals: Parameter extraction errors due to inaccurate template waveforms, Phys. Rev. D **76**, 104018 (2007).

[53] Sajad A. Bhat, Pankaj Saini, Marc Favata, and K. G. Arun, Systematic bias on the inspiral-merger-ringdown consistency test due to neglect of orbital eccentricity, Phys. Rev. D **107**, 024009 (2023).

[54] Purnima Narayan, Nathan K. Johnson-McDaniel, and Anuradha Gupta, Effect of ignoring eccentricity in testing general relativity with gravitational waves, Phys. Rev. D **108**, 064003 (2023).

[55] Alessandro Nagar *et al.*, Time-domain effective-one-body gravitational waveforms for coalescing compact binaries with nonprecessing spins, tides and self-spin effects, Phys. Rev. D **98**, 104052 (2018).

[56] Alessandro Nagar, Alice Bonino, and Piero Rettegno, Effective one-body multipolar waveform model for spin-aligned, quasicircular, eccentric, hyperbolic black hole binaries, Phys. Rev. D **103**, 104021 (2021).

[57] Md Arif Shaikh, Vijay Varma, Harald P. Pfeiffer, Antoni Ramos-Buades, and Maarten van de Meent, Defining eccentricity for gravitational wave astronomy, Phys. Rev. D **108**, 104007 (2023).

[58] Teagan A. Clarke, Isobel M. Romero-Shaw, Paul D. Lasky, and Eric Thrane, Gravitational-wave inference for eccentric binaries: The argument of periapsis, Mon. Not. R. Astron. Soc. **517**, 3778 (2022).

[59] Fabian Hofmann, Enrico Barausse, and Luciano Rezzolla, The final spin from binary black holes in quasi-circular orbits, Astrophys. J. Lett. **825**, L19 (2016).

[60] James Healy and Carlos O. Lousto, Remnant of binary black-hole mergers: New simulations and peak luminosity studies, Phys. Rev. D **95**, 024037 (2017).

[61] Xisco Jiménez-Forteza, David Keitel, Sascha Husa, Mark Hannam, Sebastian Khan, and Michael Pürrer, Hierarchical data-driven approach to fitting numerical relativity data for nonprecessing binary black holes with an application to final spin and radiated energy, Phys. Rev. D **95**, 064024 (2017).

[62] Thierry Mora and Clifford M. Will, Numerically generated quasiequilibrium orbits of black holes: Circular or eccentric?, Phys. Rev. D **66**, 101501 (2002).

[63] Antoni Ramos-Buades, Sascha Husa, Geraint Pratten, Héctor Estellés, Cecilio García-Quirós, Maite Mateu-Lucena, Marta Colleoni, and Rafel Jaume, First survey of spinning eccentric black hole mergers: Numerical relativity simulations, hybrid waveforms, and parameter estimation, Phys. Rev. D **101**, 083015 (2020).

[64] Tousif Islam, Vijay Varma, Jackie Lodman, Scott E. Field, Gaurav Khanna, Mark A. Scheel, Harald P. Pfeiffer, Davide Gerosa, and Lawrence E. Kidder, Eccentric binary black hole surrogate models for the gravitational waveform and remnant properties: Comparable mass, nonspinning case, Phys. Rev. D **103**, 064022 (2021).

[65] Antoni Ramos-Buades, Alessandra Buonanno, Mohammed Khalil, and Serguei Ossokine, Effective-one-body multipolar waveforms for eccentric binary black holes with nonprecessing spins, Phys. Rev. D **105**, 044035 (2022).

[66] Alice Bonino, Rossella Gamba, Patricia Schmidt, Alessandro Nagar, Geraint Pratten, Matteo Breschi, Piero Rettegno, and Sebastiano Bernuzzi, Inferring eccentricity evolution from observations of coalescing binary black holes, Phys. Rev. D **107**, 064024 (2023).

[67] Antoni Ramos-Buades, Maarten van de Meent, Harald P. Pfeiffer, Hannes R. Rüter, Mark A. Scheel, Michael Boyle, and Lawrence E. Kidder, Eccentric binary black holes: Comparing numerical relativity and small mass-ratio perturbation theory, Phys. Rev. D **106**, 124040 (2022).

[68] Gregory Ashton *et al.*, BILBY: A user-friendly Bayesian inference library for gravitational-wave astronomy, Astrophys. J. Suppl. Ser. **241**, 27 (2019).

[69] Joshua S. Speagle, dynesty: A dynamic nested sampling package for estimating Bayesian posteriors and evidences, Mon. Not. R. Astron. Soc. **493**, 3132 (2020).

[70] Alessandro Nagar, Piero Rettegno, Rossella Gamba, and Sebastiano Bernuzzi, Effective-one-body waveforms from dynamical captures in black hole binaries, Phys. Rev. D **103**, 064013 (2021).

[71] Danilo Chiaramello and Alessandro Nagar, Faithful analytical effective-one-body waveform model for spin-aligned, moderately eccentric, coalescing black hole binaries, Phys. Rev. D **101**, 101501 (2020).

[72] Simone Albanesi, Alessandro Nagar, and Sebastiano Bernuzzi, Effective one-body model for extreme-mass-ratio spinning binaries on eccentric equatorial orbits: Testing

radiation reaction and waveform, Phys. Rev. D **104**, 024067 (2021).

[73] Alessandro Nagar and Piero Rettegno, Next generation: Impact of high-order analytical information on effective one body waveform models for noncircularized, spin-aligned black hole binaries, Phys. Rev. D **104**, 104004 (2021).

[74] Alessandro Nagar, Rossella Gamba, Piero Rettegno, Veronica Fantini, and Sebastiano Bernuzzi, Effective-one-body waveform model for non-circularized, planar, coalescing black hole binaries: The importance of radiation reaction, arXiv:2404.05288.

[75] Antoni Ramos-Buades, Alessandra Buonanno, and Jonathan Gair, Bayesian inference of binary black holes with inspiral-merger-ringdown waveforms using two eccentric parameters, Phys. Rev. D **108**, 124063 (2023).

[76] Zhoujian Cao and Wen-Biao Han, Waveform model for an eccentric binary black hole based on the effective-one-body-numerical-relativity formalism, Phys. Rev. D **96**, 044028 (2017).

[77] Xiaolin Liu, Zhoujian Cao, and Lijing Shao, Validating the effective-one-body numerical-relativity waveform models for spin-aligned binary black holes along eccentric orbits, Phys. Rev. D **101**, 044049 (2020).

[78] Sashwat Tanay, Maria Haney, and Achamveedu Gopakumar, Frequency and time domain inspiral templates for comparable mass compact binaries in eccentric orbits, Phys. Rev. D **93**, 064031 (2016).

[79] Gregorio Carullo, Simone Albanesi, Alessandro Nagar, Rossella Gamba, Sebastiano Bernuzzi, Tomas Andrade, and Juan Trenado, Unveiling the merger structure of black hole binaries in generic planar orbits, Phys. Rev. Lett. **132**, 101401 (2024).

[80] Rossella Gamba, Matteo Breschi, Gregorio Carullo, Simone Albanesi, Piero Rettegno, Sebastiano Bernuzzi, and Alessandro Nagar, GW190521 as a dynamical capture of two nonspinning black holes, Nat. Astron. **7**, 11 (2023).

[81] Alice Bonino, Patricia Schmidt, and Geraint Pratten, Mapping eccentricity evolutions between numerical relativity and effective-one-body gravitational waveforms, arXiv:2404.18875.

[82] Nihar Gupte *et al.*, Evidence for eccentricity in the population of binary black holes observed by LIGO-Virgo-KAGRA, arXiv:2404.14286.

[83] Charlie Hoy and Vivien Raymond, PESummary: The code agnostic parameter estimation summary page builder, SoftwareX **15**, 100765 (2021).

[84] J. B. Carlin, H. S. Stern, D. B. Dunson, A. Vehtari, D. B. Rubin, and A. Gelman, *Bayesian Data Analysis* (CRC Press, New York, 2013), 10.1201/b16018.

[85] R. Abbott *et al.* (LIGO Scientific and Virgo Collaborations), Tests of general relativity with binary black holes from the second LIGO-Virgo gravitational-wave transient catalog, Phys. Rev. D **103**, 122002 (2021).